Draft version January 5, 2017
Preprint typeset using LaTeX style AASTeX6 v. 1.0

arXiv:1701.00884v1 [astro-ph.HE] 4 Jan 2017

ORIGIN OF THE GALACTIC DIFFUSE X-RAY EMISSION: IRON K-SHELL LINE DIAGNOSTICS

Masayoshi Nobukawa[1], Hideki Uchiyama[2], Kumiko K. Nobukawa[3,4], Shigeo Yamauchi[4], and Katsuji Koyama[3,5]

[1]Department of Teacher Training and School Education, Nara University of Education, Takabatake-cho, Nara, 630-8528, Japan
nobukawa@nara-edu.ac.jp
[2]Faculty of Education, Shizuoka University, 836 Ohya, Suruga-ku, Shizuoka, 422-8529, Japan
[3]Department of Physics, Graduate School of Science, Kyoto University, Kitashirakawa-oiwake-cho, Sakyo-ku, Kyoto, 606-8502, Japan
[4]Department of Physics, Nara Women's University, Kitauoyanishimachi, Nara, 630-8506, Japan

ABSTRACT

This paper reports detailed K-shell line profiles of iron (Fe) and nickel (Ni) of the Galactic Center X-ray Emission (GCXE), Galactic Bulge X-ray Emission (GBXE), Galactic Ridge X-ray Emission (GRXE), magnetic Cataclysmic Variables (mCVs), non-magnetic Cataclysmic Variables (non-mCVs), and coronally Active Binaries (ABs). For the study of the origin of the GCXE, GBXE, and GRXE, the spectral analysis is focused on equivalent widths of the Fe I-Kα, Fe XXV-Heα, and Fe XXVI-Lyα lines. The global spectrum of the GBXE is reproduced by a combination of the mCVs, non-mCVs, and ABs spectra. On the other hand, the GRXE spectrum shows significant data excesses at the Fe I-Kα and Fe XXV-Heα line energies. This means that additional components other than mCVs, non-mCVs, and ABs are required, which have symbiotic phenomena of cold gas and very high-temperature plasma. The GCXE spectrum shows larger excesses than those found in the GRXE spectrum at all the K-shell lines of iron and nickel. Among them the largest ones are the Fe I-Kα, Fe XXV-Heα, Fe XXVI-Lyα, and Fe XXVI-Lyβ lines. Together with the fact that the scale heights of the Fe I-Kα, Fe XXV-Heα, and Fe XXVI-Lyα lines are similar to that of the central molecular zone (CMZ), the excess components would be related to high-energy activity in the extreme envelopment of the CMZ.

Keywords: Galaxy: center — Galaxy: disk — Galaxy: bulge — X-rays: ISM —X-rays: stars

1. INTRODUCTION

The Galactic Diffuse X-ray Emission (GDXE) is unresolved X-rays prevailing over the Galactic plane (e.g. Worrall et al. 1982). One of the most remarkable features of the GDXE is strong K-shell lines of neutral (Fe I-Kα), helium-like (Fe XXV-Heα), and hydrogen-like irons (Fe XXVI-Lyα) at 6.40 keV, 6.68 keV, and 6.97 keV, respectively (Koyama et al. 1996, 2007d; Yamauchi et al. 2009). The GDXE is decomposed into the Galactic Center X-ray Emission (GCXE), the Galactic Bulge X-ray Emission (GBXE), and the Galactic Ridge X-ray Emission (GRXE) (Koyama et al. 1989; Yamauchi and Koyama 1993; Uchiyama et al. 2013; Yamauchi et al. 2016). Although the global X-ray spectra of the GCXE, GBXE, and GRXE are similar to each other, the detailed structures, particularly the iron K-shell line structures are significantly different (Yamauchi et al. 2016).

Since the discovery of the GDXE, its origin, whether unresolved point sources or truly diffuse plasma, has been under debate for a long time. In the point source scenario, the candidate stars have been mainly Cataclysmic Variables (CVs) and coronally Active Binaries (ABs) with their reasonable number densities, high-temperature plasma, and strong iron K-shell lines (Revnivtsev et al. 2009; Warwick 2014). The previous debates around the point source origin have been based on two observational facts that (1) the longitude distributions of the continuum (e.g. 2–10 keV band) and the iron K-shell line fluxes resemble to the infrared surface brightness distribution (Revnivtsev et al. 2006a,b), which is regarded as a tracer of the stellar mass distribution (SMD), and (2) the flux of the resolved point sources is roughly equal to the total GDXE flux, if the reliable point source flux in the luminosity range of $\gtrsim 10^{31}$ erg s^{-1} is extrapolated to the low-luminosity limit of $\sim 10^{28}$ erg s^{-1} using empirically made X-ray luminosity functions (XLFs) (Sazonov et al. 2006; Revnivtsev et al. 2009; Warwick 2014).

These processes, however, have large observational uncertainty. In (1), both the X-ray and infrared SMDs are made with poor spatial sub-degree resolution. Therefore, the fine profiles of the GCXE of $\sim 1^\circ.2 \times 0^\circ.5$ size, and the boundaries between the GCXE, GBXE, and GRXE are smeared out. The latitude distribution of the GDXE flux is not also determined precisely. The

infrared surface brightness distribution is a tracer of the star distribution including high-mass objects, but it is not clear how correctly it traces the distribution of low-mass stars such as CVs and ABs. In (2), the XLFs are made by limited sample numbers, luminosity range, and spectral information of candidate point sources, and hence have large errors of $\gtrsim$50% (e.g. Sazonov et al. 2006). In fact, the XLFs are largely different from author to author (Revnivtsev et al. 2009; Hong 2012; Warwick 2014). In addition, the resolved fraction, even in the reliable luminosity range of $\gtrsim 10^{31}$ erg s^{-1}, is typically $\sim$10–30% with uncertainty of factor of ~ 3.

In the examination of the GDXE origin, whether from point sources, truly diffuse plasma or other origins, equivalent widths (EWs) of Fe I-Kα (EW$_{6.40}$), Fe XXV-Heα (EW$_{6.68}$), and Fe XXVI-Lyα (EW$_{6.97}$) of the GDXE, magnetic CVs (mCVs), non-magnetic CVs (non-mCVs), and ABs are key factors. The limited energy resolutions of previous observations cannot separate the iron K-shell lines into Fe I-Kα, Fe XXV-Heα and Fe XXVI-Lyα, and hence the EWs of the GCXE, GBXE, and GRXE have not been accurate enough. In addition, the EWs of mCVs, non-mCVs and ABs have also been very limited, with large errors or significant variations from author to author, and/or from instrument to instrument. The best-quality global spatial and spectral structures of the GCXE, GBXE, and GRXE, and high-quality spectra of mCVs, non-mCVs, and ABs become available from the *Suzaku* observations: see Koyama et al. (2007b); Uchiyama et al. (2011) for the GDXE, and Xu et al. (2016) for mCVs, non-mCVs and ABs.

The motivation of this work is to try different diagnostics from the previous methods for the origins of the GCXE, GBXE, and GRXE. Our new diagnostics is to use high-quality spectra with accurate EW$_{6.40}$, EW$_{6.68}$, and EW$_{6.97}$ from the GCXE, GBXE, GRXE, mCVs, non-mCVs, and ABs, which are obtained from all the *Suzaku* archives. This approach is applied partly by Xu et al. (2016), and this paper intends to further extend their method.

The contents of this paper is as follows. The observations and data reductions are described in section 2. The EWs of the K-shell lines of iron and nickel from mCVs, non-mCVs, ABs, and the GDXE obtained from all the available *Suzaku* archives are presented in sections 3.1 and 3.2. Mean spectra of mCVs, non-mCVs, and ABs are constructed in sections 3.3 and 3.4. In section 3.5, we fit the GDXE spectra with a combination of the mean spectra, focusing on the K-shell line structures. Using the results, the origins of the GCXE, GRXE, and GBXE are separately discussed in section 4.

2. OBSERVATIONS AND DATA REDUCTION

The *Suzaku* archives are the data taken in the full mission life of *Suzaku* from 2005 to 2015. We used the X-ray Imaging Spectrometers (XIS, Koyama et al. 2007a) placed on the focal planes of the thin-foil X-ray telescopes (Serlemitsos et al. 2007). The XIS consists of four sensors: XIS sensor-1 (XIS 1) has a back-illuminated CCD, while the other three XIS sensors (XIS 0, 2, and 3) have front-illuminated CCDs. XIS 2 turned dysfunctional, and hence the other three sensors (XIS 0, 1, and 3) have been operated since 2006 November 9. A small fraction of the XIS 0 area has not been used since 2009 June 23 because of the damage by a possible micro-meteorite. The XIS has been operated in the normal clocking mode. The field of view of the XIS is $17'.8 \times 17'.8$.

Data reduction and analysis were carried out using the HEAsoft version 6.17. The XIS pulse-height data for each X-ray event were converted to pulse invariant channels using the `xispi` software and the calibration database. The data obtained at the South Atlantic Anomaly, during Earth occultation, and at low elevation angles from the Earth rim of $< 5°$ (night Earth) or $< 20°$ (day Earth) were excluded. After removing hot and flickering pixels, the events of grade 0, 2, 3, 4, and 6 were used.

3. ANALYSIS AND RESULTS

3.1. *X-ray spectra of the GCXE, GBXE, and GRXE*

Following the results of Uchiyama et al. (2013) and Yamauchi et al. (2016), we selected the data of the GCXE, GBXE, and GRXE from the ($|l_*| < 0°.6$, $|b_*| < 0°.25$), ($|l_*| < 0°.6$, $1° < |b_*| < 3°$) and ($|l_*| = 10°$–$30°$, $|b_*| < 1°$) regions, respectively. Here we define a new coordinate of $l_* = l + 0°.056$ and b_*=$b + 0°.046$, where the position of Sagittarius (Sgr) A* is given by $(l_*, b_*) = (0°, 0°)$ (Reid & Brunthaler 2004). To obtain the pure GCXE spectrum, bright Fe I-Kα and Fe XXV-Heα spots of Sgr A, B, C, Sgr A East, and the Arches Cluster (Koyama et al. 2007b,c; Tsujimoto et al. 2007; Nakajima et al. 2009; Nobukawa et al. 2010), and bright LMXBs (1E 1743.1−2843 and AX J1744.8−2921, Vaiana et al. 1981; Sakano et al. 2002) were excluded. The region of the GCXE is shown in figure 1. The total exposure times are $\sim$1.3 Ms, $\sim$800 ks, and $\sim$3.0 Ms, for the GCXE, GBXE, and GRXE, respectively.

We then made raw spectra from all the GCXE, GBXE, and GRXE regions. The non-X-ray background (NXB) was subtracted using the `xisnxbgen` software (Tawa et al. 2008). We fit the NXB-subtracted spectra with a phenomenological model consisting of a bremsstrahlung continuum, an iron K-shell absorption edge (`edge` in XSPEC), and many Gaussian lines plus the cosmic X-ray background (CXB). The Gaussian line

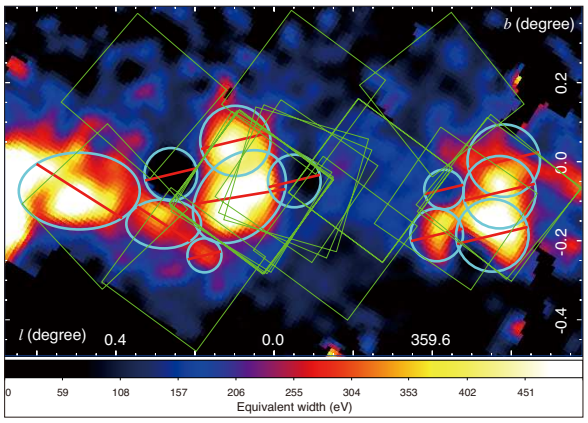

Figure 1. The regions of the GCXE spectrum overlaid on the Fe I-Kα EW map. The spectrum of the GCXE is extracted from the green squares excluding the light blue circles.

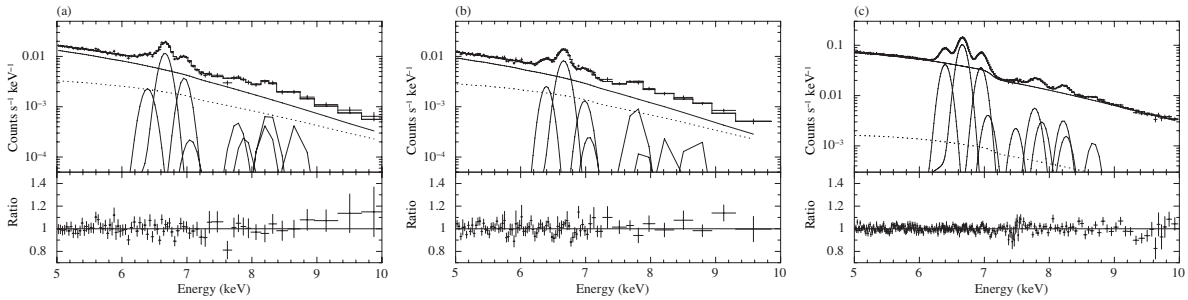

Figure 2. GDXE spectra for the GBXE (a), GRXE (b), and GCXE (c). The spectra are fitted with a phenomenological model consisting of bremsstrahlung and ten Gaussians with intersteller absorption. The CXB is added with the dotted model. The best-fit parameters are listed in table 1.

energies are taken from the AtomDB 3.0.2[1], while the widths of the Fe XXV-Heα lines and the others are fixed to ~ 30 eV and $\sim$0 eV, respectively.

The CXB is given by a power-law function with fixed photon index and flux of 1.4 and 8.2×10^{-7} photons s^{-1} cm^{-2} arcmin^{-2} keV^{-1} at 1 keV, respectively (Kushino et al. 2002). The best-fit results are shown in figure 2, while the best-fit parameters are listed in table 1.

The ratio of Fe XXVI-Lyα/Fe XXV-Heα of the GCXE, GBXE, and GRXE are 0.37 ± 0.02, 0.34 ± 0.03, and 0.17 ± 0.02, which correspond to the collisional ionization equilibrium (CIE) temperatures of $\sim$ 6.8, $\sim$ 6.5, and $\sim$ 5.0 keV, respectively. Thus, the temperatures of the GCXE, GBXE, and GRXE are not significantly different from each other. However, the continuum shape of the GCXE gives the bremsstrahlung temperature of $\sim$15 keV, which is significantly larger than those of the GBXE and GRXE of $\sim$5 keV (table 1). This apparent inconsistency in the temperatures would be due to different flux ratio of the hard X-ray spectra associated to the Fe I-Kα line (cold gas component) relative to the high-temperature plasma associated with Fe XXV-Heα and Fe XXVI-Lyα line. In fact, the flux ratio of Fe I-Kα/Fe XXV-Heα in the GCXE is 0.38 ± 0.02, which is significantly larger than those of the GBXE and GRXE of 0.20 ± 0.03 and 0.27 ± 0.02, respectively.

[1] http://www.atomdb.org/

3.2. *Sample of mCVs, non-mCVs, and ABs*

We selected the sample sources of intermediate polars (IPs), polars (Ps), symbiotic stars (SSs), non-mCVs (dwarf novae), and ABs from table 1 of Xu et al. (2016). The IPs, Ps, and SSs were combined into a single class of mCVs, because the number densities of Ps and SSs are smaller than IPs (Patterson 1984), and the X-ray spectra are similar to each other, compared with those of non-mCVs and ABs. From the spectral features, we classify GK per to a mCV (IP) instead of a non-mCV, and omit BF Ori from the list of non-mCV (see Sheets et al. 2007; Neustroev & Zharikov 2008).

For the ABs, we added other sources of Algol (OBSID=401093010), EV Lac (402032010), HR 9024 (401032010), HD130693 (405031010), and β Lyr (401036010, 401036020, 401036030). The sample names of mCVs, non-mCVs, and ABs in this paper are listed in table 2.

We make spectra of the samples, and fit with a CIE

Table 1. The best-fit parameters of the GDXE.

	GBXE		GRXE		GCXE	
Continuum						
$N_{\rm H}$ (10^{22} cm^{-2})	3 (fix)		3 (fix)		6 (fix)	
Fe K edge[a]	0 (fix)		0 (fix)		0.24 ± 0.01	
$kT_{\rm e}$ (keV)	5.1 ± 0.4		5.0 ± 0.4		$14.9^{+0.5}_{-0.6}$	
flux [b]	8.6×10^{-15}		7.3×10^{-15}		1.1×10^{-13}	
Emission lines						
Line[c]	CE[c]	Flux[d]	EW[e]	Flux[d]	EW[e]	Flux[d]	EW[e]
FeI-Kα	6400	0.14±0.02	84±10	0.16±0.01	118±9	3.54±0.04	175±2
FeXXV-Heα	6680	0.70±0.02	463±13	0.60±0.02	487±13	9.40±0.05	500±3
FeXXVI-Lyα	6966	0.24±0.02	173±13	0.10±0.01	96±11	3.45±0.04	198±2
FeI-Kβ	7059	0.01[f]	14	0.02[f]	19	0.44[f]	26
NiI-Kα	7490	—	—	—	—	0.37±0.07	24±5
NiXXVII-Heα	7771	0.05 ± 0.03	53±31	0.14±0.03	173±36	1.10±0.06	78±4
FeXXV-Heβ	7881	< 0.06	< 61	< 0.06	< 76	0.61±0.06	45±4
FeXXVI-Lyβ	8251	< 0.13	< 101	< 0.09	< 97	0.74±0.12	54±9
FeXXV-Heγ	8295	0.11 ± 0.08	130^{+92}_{-98}	0.06 ± 0.03	86 ± 44	0.38±0.13	30±10
FeXXVI-Lyγ	8700	0.09±0.03	120±41	0.08±0.03	147±49	0.34±0.05	30±4
χ^2/d.o.f.	117/84		107/72		331/265	

Errors are one standard deviation (1 σ).

[a] Absorption depth at 7.11 keV.

[b] Absorption-corrected flux in the unit erg s^{-1} cm^{-2} arcmin^{-2}. The CXB is not included.

[c] AtomDB 3.0.2 (http://www.atomdb.org/) and Wargelin et al. (2005). Unit is eV.

[d] Unit is 10^{-7} photon cm^{-2} s^{-1} arcmin^{-2}.

[e] Unit is eV.

[f] Fixed to 0.125×FeI-Kα.

Table 2. List of active stars used in this work.

Magnetic CV (mCV)
Symbiotic Stars(SS): CH Cyg, RS Oph, RT Cru, SS73-17, T CrB, V407 Cyg
Intemediate polar(IP): AO Psc, BG Cmi, EX Hya, FO Aqr, GK Per, IGR J17195−4100, IGR J17303−0601, MU Cam, NY Lup, PQ Gem, TV Col, TX Col, V1223 Sgr, 1RXS J213344.1+51072, V2400 Oph, V709 Cas, XY Ari
Polar(P): AM Her, V1432 Aql, SWIFT J2319.4+2619
Non-magnetic CV (non-mCV)
BV Cen, BZ UMa, EK TrA, FL Psc, FS Aur, KT Per, SS Aur, SS Cyg, U Gem, V1159 Ori, V893 Sco, VW Hyi, VY Aqr, Z Cam
Active Binary (AB)
GT Mus, Algol, II Peg, σ Gem, UX Ari, EV Lac, HR 9024, β Lyr, HD 130693

Observation sequence numbers of the sources are referred to Xu et al. (2016) except for Algol, EV Lac, HR 9024, HD130693, and β Lyr (see text).

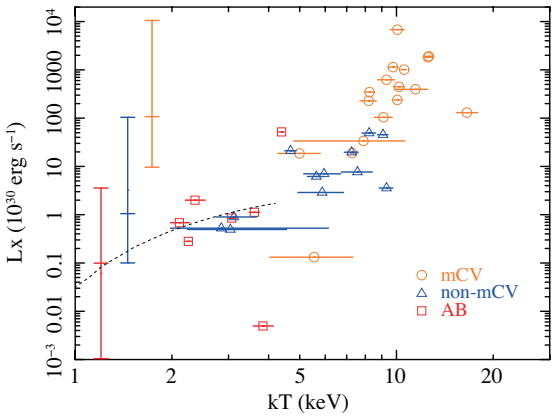

Figure 3. kT and L_X plot of point sources. The mCVs, non-mCVs, and ABs are shown with orange circle, blue triangle, and red square, respectively. The dashed line shows a model curve of kT and L_X calculated by APEC, which is used for ABs (see section 3.4). The vertical bars show the groups we divided to make Model B (see section 3.4 and table 4).

plasma (APEC) model. Free parameters are temperature kT, iron abundance Z_{Fe}, and luminosity L_X in 5–10 keV. We used distances of the point sources shown in table 1 of Xu et al. (2016) (references therein) to convert fluxes into luminosities. Figure 3 shows a positive correlation between kT and L_X. The data of mCVs and non-mCVs distribute in the range of $L_X \sim 10^{31-34}$ erg s^{-1} and 10^{29-32} erg s^{-1} corresponding to $kT \sim$ 5–15 keV and 3–10 keV, respectively. For ABs, except for two samples with large dispersion in $L_X \lesssim 10^{28}$ erg s^{-1} and $\sim 10^{32}$ erg s^{-1}, the luminosity L_X and temperature kT are $10^{29-30.5}$ erg s^{-1} and 2–4 keV, respectively

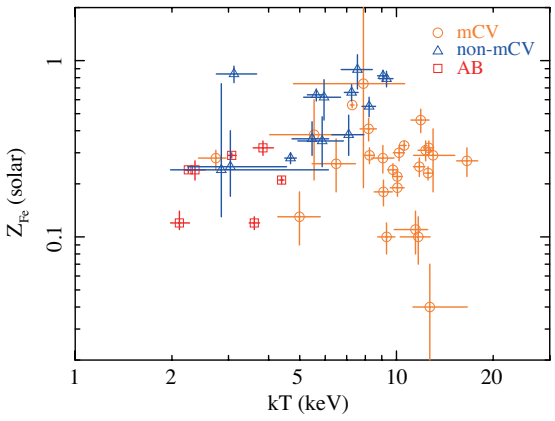

Figure 4. kT and Z_{Fe} plot of point sources with the same symbols as figure 3.

On the other hand, no clear correlation is seen between kT and Z_{Fe} (figure 4). The mean abundance Z_{Fe} and the standard deviation of mCVs, non-mCVs, and ABs are estimated to be 0.28 ± 0.16 solar, 0.58 ± 0.24 solar, and 0.22 ± 0.08 solar, respectively. The physical reason for this apparent difference of the mean abundances among mCVs, non-mCVs and ABs is not fully understood, but would be related to the different production mechanism of the hot plasmas; the hot plasmas are produced by the shock of a freefall velocity on the white dwarf surface (mCVs), Keplerian velocity near the white dwarf surface (non-mCVs), and coronal activity (ABs).

3.3. *Mean X-ray spectra of mCVs, non-mCVs, and ABs (Model A)*

We co-added each source spectra in table 2, where each spectra are converted to those at the same distance of 8 kpc (hereafter, the mean spectra). The mean spectra of the mCVs, non-mCVs, and ABs are shown in figure 5. The CXB was subtracted from the spectra. Then we fit the spectra by the same phenomenological model as section 3.1. The best fit models are given in the solid line of figure 5, while the best-fit parameters are listed in table 3. Parameters of SSs, IPs, and Ps, which are the subclasses of mCVs, are also shown in the table. Hereafter, we call these mean spectra Model A.

The Model A may not fully present the mean spectra of mCVs, non-mCVs, and ABs, because the samples are limited in the luminosity ranges of $L_X \sim 10^{31-34}$ erg s^{-1}, $\sim 10^{29-32}$ erg s^{-1}, and $\sim 10^{29-30.5}$ erg s^{-1} (5–10 keV), for the mCVs, non-mCVs, and ABs, respectively (figure 3). Contribution of samples with low luminosity is possibly underestimated due to the detection bias. Since the sources in the luminosity range of $\lesssim 10^{29-30}$ erg s^{-1} may contribute non-negligible fractions in the mean spectra, we try to include the possible contribution of low-luminosity sources to the mean spectra of the mCVs, non-mCVs, and ABs in the next section (Model B).

3.4. *Mean X-ray spectra of mCVs, non-mCVs, and ABs (Model B)*

Since the Fe XXV-Heα, and Fe XXVI-Lyα structure in the mCV, non-mCV, and AB spectra are well represented by a thermal plasma (e.g., mCVs: Yuasa et al. 2012, non-mCVs: Byckling et al. 2010, ABs: Pandey & Singh 2012), we fit the observed spectra of individual sources with a model of CIE plasma (APEC) plus Fe I-Kα, Fe I-Kβ, and Ni I-Kα lines given by Gaussians. Using the best-fit model, we estimated $EW_{6.68}$ and $EW_{6.97}$.

Figure 6 shows a correlation plot between kT and $EW_{6.40}$. The $EW_{6.40}$ depends on the geometry and N_H of the cold gas near and around the hot plasma. If we assume that the geometry and N_H of the cold gas around the hot plasma are the same in all the sources, the $EW_{6.40}$ becomes a simple function of kT; $EW_{6.40}$ is roughly proportional to the Fe I-Kα flux divided by the fluxes at above the Fe-K edge energy. The dotted and dashed lines in figure 6 are the simulated results of the

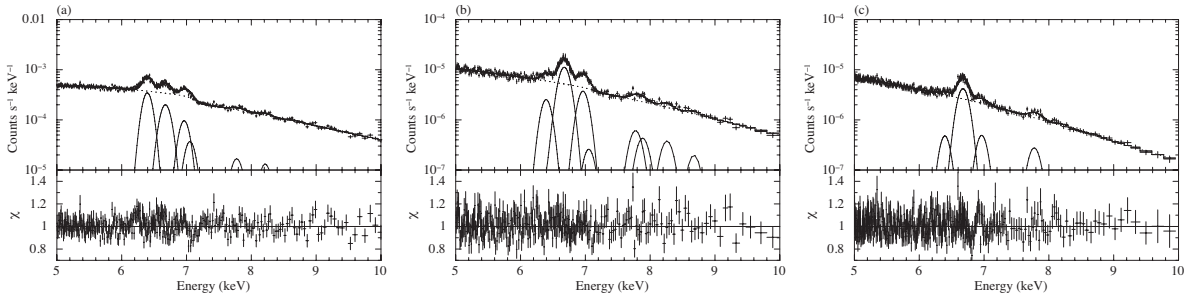

Figure 5. Averaged spectra of mCVs, non-mCVs, ABs for Model A (see section 3.3), which are normalized as a point source located at 8 kpc.

Table 3. Best-fit parameters of mCVs (SSs+IPs+Ps), SSs, IPs, Ps, non-mCVs, and ABs for Model A.

	mCV		SS		IP		P		non-mCV		AB	
Continuum												
$N_{\rm H}$ (10^{22} cm^{-2})	14.7±1.5		18.0±2.3		9.7±0.4		12.7±3.4		0 (fix)		0 (fix)	
Fe K edge[a]	0.05 ± 0.01		< 0.07		0.02 ± 0.01		0.10 ± 0.06		0.08 ± 0.04		0.02(< 0.05)	
$kT_{\rm e}$ (keV)	$23.3^{+5.1}_{-3.7}$		$24.5^{+5.3}_{-5.8}$		18.7 ± 0.6		$25.7^{+20.7}_{-8.0}$		10.7±1.7		4.25 ± 0.18	
flux (erg s^{-1} cm^{-2})[b]	1.1×10^{-13}		2.5×10^{-13}		6.3×10^{-14}		8.0×10^{-15}		1.6×10^{-15}		7.8×10^{-16}	
Emission lines												
Line[c]	CE[c]	Flux[d] 10^{-7}	EW[e]	Flux[d] 10^{-6}	EW[e]	Flux[d] 10^{-7}	EW[e]	Flux[d] 10^{-8}	EW[e]	Flux[d] 10^{-8}	EW[e]	Flux[d] 10^{-9}	EW[e]
FeI-Kα	6400	4.88±0.13	169±5	1.36±0.05	194±7	1.90±0.04	124±5	2.44±0.22	116±10	0.26±0.02	82±7	0.49±0.09	28±5
FeXXV-Heα	6680	3.19±0.12	118±5	0.82±0.05	118±7	1.63±0.04	114±5	2.30±0.22	117±11	1.29±0.03	451±10	4.97±0.12	327±8
FeXXVI-Lyα	6966	1.52±0.11	60±4	0.37±0.04	60±7	0.89±0.03	67±4	0.70±0.20	38±11	0.44±0.02	167±9	0.60±0.09	45±6
FeI-Kβ	7059	0.61[f]	25	0.17[f]	25	0.24[f]	18	0.30[f]	17	0.07[f]	12	0.06[f]	5
NiI-Kα	7490	-	-	-	-	-	-	-	-	-	-	-	-
NiXXVII-Heα	7771	0.48±0.17	23±8	$0.17^{+0.05}_{-0.03}$	34^{+10}_{-6}	< 0.08	< 8	< 0.27	< 33	0.12±0.03	56±14	0.53±0.13	55±13
FeXXV-Heβ	7881	< 0.32	< 16	< 0.06	< 12	0.18 ± 0.05	17 ± 5	$0.50^{+0.23}_{-0.29}$	33^{+15}_{-19}	0.09±0.03	43±14	0.15±0.13	17±15
FeXXVI-Lyβ	8251	$0.43^{+0.13}_{-0.33}$	22^{+7}_{-17}	$0.12^{+0.05}_{-0.09}$	25^{+10}_{-19}	< 0.07	< 6	< 0.55	< 35	< 0.07	< 28	0.16±0.10	20±14
FeXXV-Heγ	8295	< 0.35	< 18	< 0.08	< 17	$0.20^{+0.04}_{-0.07}$	20^{+4}_{-7}	< 0.58	< 40	$0.09^{+0.03}_{-0.07}$	50^{+17}_{-39}	< 0.08	< 13
FeXXVI-Lyγ	8700	0.18 ± 0.13	10 ± 7	< 0.10	< 24	0.05 ± 0.04	5 ± 4	< 0.43	< 33	0.06±0.03	34±17	< 0.17	< 24
χ^2/d.o.f.		409/314		363/302		735/610		109/130		297/274		361/363	

Errors are one standard deviation (1 σ).

[a] Absorption depth at 7.11 keV.

[b] Flux at 8 kpc in the 5–10 keV band per a source.

[c] AtomDB 3.0.2 (http://www.atomdb.org/) and Wargelin et al. (2005). Unit is eV.

[d] Unit is photon cm^{-2} s^{-1}.

[e] Unit is eV.

[f] Fixed to 0.125×FeI-Kα.

kT vs EW$_{6.40}$ relation, where EW$_{6.40}$ is produced by the irradiation of X-rays from a plasma on the cold gas with temperature of kT and gas density of $N_{\rm H}$. As is shown in figure 6, data of CVs (mCV+non-mCV) and ABs are well fitted with the model curve of $N_{\rm H} = 1 \times 10^{23}$ cm^{-2} (dashed line) and 3×10^{22} cm^{-2} (dotted line), respectively.

The correlation plot of EW$_{6.68}$ divided by $Z_{\rm Fe}$ as a function of kT is given in figure 7. The dashed curve is a simulated result for a thermal plasma. The results well reproduce the observed EW$_{6.68}/Z_{\rm Fe}$, which supports our initial assumption that the spectra of mCV, non-mCV, and ABs are all well approximated by a simple CIE plasma model at least in the energy band of 5–10 keV.

Using the results in figures 3 and 6, and adopting the mean $Z_{\rm Fe}$ of each category (section 3.2), we can incorporate the XLF effect into the mean spectra as a form of multi-kT, $Z_{\rm Fe}$, and EW$_{6.40}$ spectra. However, for simplicity, we construct a two-representative (two kT and EW$_{6.40}$) plasma as a good approximation of multi-temperature and EW$_{6.40}$ structure.

For mCVs, we refer to the XLF provided by Warwick (2014), where essentially all the source are in our range of 10^{31}–10^{34} erg s^{-1}. We are focusing on the 5–10 keV luminosity, which is different from the 2–10 keV band used by Warwick (2014). We calculated conversion fac-

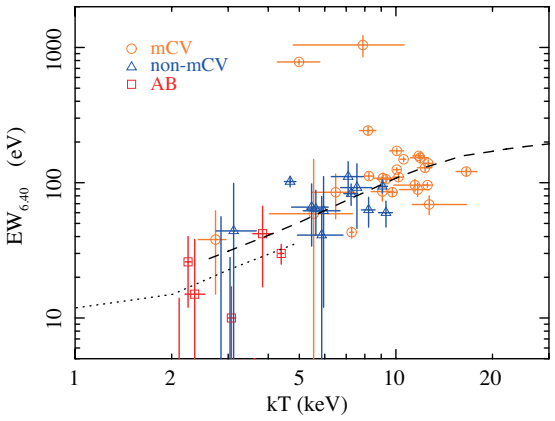

Figure 6. kT and $EW_{6.40}$ plot of point sources with the same symbols as figure 3. The dashed and dotted curves show simulated results, where $EW_{6.40}$ is produced by irradiated X-rays from a plasma on the cold gas with $N_H = 1 \times 10^{23}$ cm^{-2} and 3×10^{22} cm^{-2} for CVs (mCVs + non-mCVs) and ABs, respectively.

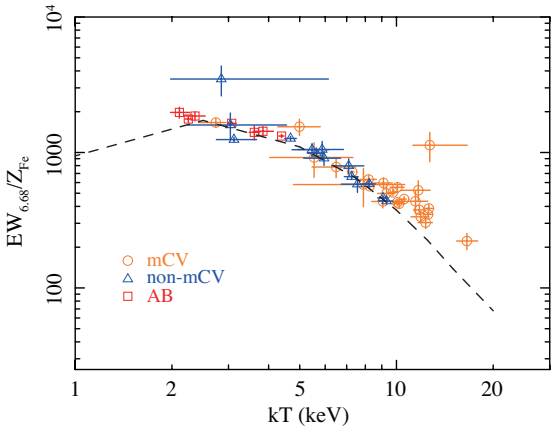

Figure 7. kT and $EW_{6.68}/Z_{Fe}$ plot of point sources with the same symbols as figure 3. A simulated model that is derived from the APEC code is shown with the dashed curve.

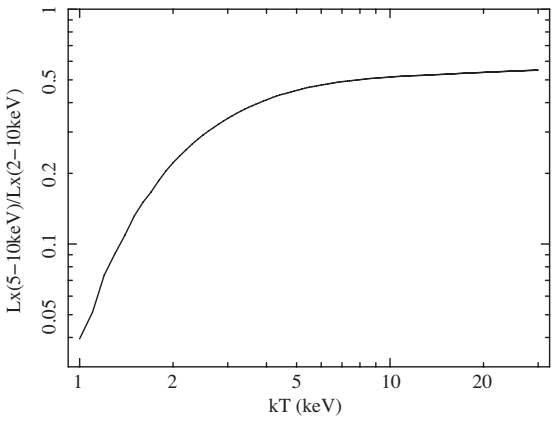

Figure 8. kT and L_X ratio between 5–10 keV and 2–10 keV bands.

tor between the 2–10 keV and 5–10 keV luminosities using APEC model with various kT (figure 8), and modified the XLF for the 5–10 keV band (hear and after the modified XLF). We, then, divided mCVs data into two groups of 10^{31-32} erg s^{-1} and 10^{32-34} erg s^{-1}. The equivalent kT ranges are 7 and 10 keV (see figure 3). We also calculated that the luminosity ratio between these luminosity bands are 0.98 : 1 based on the modified XLF. Taking these representative kTs, we made a two-kT and $EW_{6.40}$ spectrum of mCVs (Model B) as [kT = 7 keV, $EW_{6.40}$= 80 eV] and [kT = 10 keV, $EW_{6.40}$= 110 eV] with the luminosity ratio of 0.98 : 1 (table 4).

In the same manner, the Model B spectrum for the non-mCVs is made with two components of the luminosity ranges of 10^{29-30} erg s^{-1} and 10^{30-32} erg s^{-1} with [kT = 3 keV, $EW_{6.40}$= 35 eV] and [kT = 8 keV, $EW_{6.40}$= 90 eV], respectively. Using the modified XLF, we calculated the luminosity ratio of 0.17 : 1.

The XLF of ABs is highly uncertain, but our sample of ABs would be in the highest luminosity range of $10^{29-30.5}$ erg s^{-1}, where the relevant temperature range is ∼2–4 keV. We make two groups of L_X = 10^{27-29} erg s^{-1} and $10^{29-30.5}$ erg s^{-1}. Since there is no sample in the lower luminosity group, we assume the kT–L_X relation using the CIE plasma model (APEC) (the dashed curve in figure 3). Then, the two groups have parameter sets of [kT = 1 keV, $EW_{6.40}$= 10 eV] and [kT = 3 keV, $EW_{6.40}$= 25 eV], respectively. The luminosity ratio 1.6×10^{-2} : 1 is also calculated from the modified XLF in the same manner as mCVs and non-mCVs. Although contribution of low-kT ABs of $\lesssim$2 keV may not be negligible in the 2–10 keV flux (e.g. Sazonov et al. 2006; Warwick 2014), the contribution to in the 5–10 keV band would be very small. This is because low-temperature plasma hardly emits high energy X-rays of $\gtrsim$ 5 keV. Using the parameters listed in table 4, we constructed Model B for mCVs, non-mCVs, and ABs.

Table 4. Parameters of mCVs, non-mCVs, and ABs of Model B.

		L_X (erg s^{-1})	kT (keV)	$EW_{6.40}$ (eV)	Z_{Fe} (solar)	L_X ratio[a] (low/high)
mCVs	high	10^{32-34}	10	110	0.28	—
	low	10^{31-32}	7	80	0.28	0.98
non-mCVs	high	10^{30-32}	8	90	0.58	—
	low	10^{29-30}	3	35	0.58	0.17
ABs	high	$10^{29-30.5}$	3	25	0.22	—
	low	10^{27-29}	1	10	0.22	1.6×10^{-2}

[a]Luminosity ratio in the 5–10 keV band (see text).

3.5. *Reconstruction of the GDXE spectra by assembly of point sources*

For the reconstruction of the GDXE by assembly of point sources (mCVs, non-mCVs, and ABs) , key parameters are EWs of iron (Fe I-Kα, Fe XXV-Heα, and Fe XXVI-Lyα). In the next subsections 3.5.1 and 3.5.2, we simply reconstruct the observed GDXE spectra with those of the observation-based model (Model A). However, for the reconstruction by Model B, the iron abundances in the ISMs between the solar neighbor and that near the GDXE should be taken into account, because the observed iron EWs would be proportional to the iron abundances in the relevant ISM. The iron abundance in the GDXE is nearly 1 solar in the X-ray observations (Koyama et al. 2007b; Nobukawa et al. 2010; Uchiyama et al. 2013). Also the infrared observation gives nearly 1 solar iron abundance in the ISM near the Galactic center (Cunha et al. 2007). Therefore, for the reconstruction of the GDXE by Model B, we assume the iron abundances in the solar neighborhood and that in the GDXE regions are the same, being 1 solar, and hence no abundance correction of the iron EWs in both the GDXE and Model B is made.

3.5.1. *GBXE*

Revnivtsev et al. (2009); Hong (2012) suggested that more than 80% of the GBXE flux is due to integrated point sources of CVs (mCVs and non-mCVs) and ABs. We, therefore, fit the GBXE spectrum with a combination of the mean spectra of mCVs, non-mCVs and ABs (Model A and Model B) plus the fixed CXB model. The free parameters are $F_{\rm mCV}, F_{\rm non-mCV}$, and $F_{\rm AB}$ (erg cm^{-2} s^{-1} arcmin^{-2}), which are the surface brightness of mCVs, non-mCVs, and ABs, respectively. Here, we define the parameters of fraction, $f_{\rm mCV} = F_{\rm mCV}/Sum$, $f_{\rm non-mCV} = F_{\rm non-mCV}/Sum$ and $f_{\rm AB} = F_{\rm AB}/Sum$, where Sum is $F_{\rm mCV}+F_{\rm non-mCV}+F_{\rm AB}$. The interstellar column density of $N_{\rm H}$ is fixed to 3×10^{22} cm^{-2}. The $N_{\rm H}$ value, however, has no significant effect on the best-fit parameters of the 5–10 keV band spectra. The fits are reasonably nice with χ^2/d.o.f.= 160/95 and 148/95 for the Model A and Model B, respectively, although residuals at $\sim$ 8.3 keV are seen. The best-fit results are shown in figure 9, and the mixing ratio for Model B is listed in table 5.

The fitting result suggests that the major fraction of the GBXE is due to non-mCVs. No essential difference between the Model A and Model B fit is found. We, thus, use Model B for the GRXE and GCXE spectra in the next subsection.

3.5.2. *GRXE and GCXE*

Unlike the GBXE, there are no observational facts to resolve the majority of the GRXE and GCXE flux into point sources. We, nevertheless, try to fit the GRXE and GCXE spectra by a combination of the mean spectra of mCVs, non-mCVs, and ABs (figure 10). The free parameters are the same as the GDXE but $N_{\rm H}$ are fixed to 6×10^{22} cm^{-2} and 3×10^{22} cm^{-2}, for the GRXE and GCXE, respectively. The fitting rejects that the GRXE and GCXE spectra are combinations of only mCVs, non-mCVs, and ABs, with the χ^2/d.o.f. of 282/91, and 2637/276 for the GRXE and GCXE, respectively, where large residuals are found in the 6.2–7.2 keV band. The Model B fitting also retains residuals at $\sim$ 7.6 keV in the GRXE spectrum, and at $\sim$ 7.5–7.9 keV and $\sim$ 8.2–8.3 keV in the GCXE spectrum, respectively.

Table 5. Best-fit flux ratio of mCVs, non-mCVs and ABs for Model B.

	GBXE	GRXE	GCXE
$f_{\rm mCV}$	0.03($<$ 0.09)	0.10 ± 0.05	0.04 ± 0.01
$f_{\rm non-mCV}$	0.67 ± 0.06	0.51 ± 0.06	0.96 ± 0.01
$f_{\rm AB}$	0.30 ± 0.03	0.39 ± 0.02	0.00($<$ 0.01)
χ^2/d.o.f.	148/95 (1.56)	282/91 (3.10)	2637/276 (9.55)

The main disagreement of the GRXE and GCXE spectra from the combined model of mCVs, non-mCVs, and ABs lie in the 6.2–7.2 keV band. This band includes the Fe I-Kα, Fe XXV-Heα, and Fe XXVI-Lyα lines, and hence these lines are key elements to separately diagnose the origins of the GCXE, GBXE, and GRXE (sections 4.2, 4.3, and 4.4).

4. DISCUSSION

4.1. *Equivalent Widths of the iron K-shell lines from mCVs, non-mCVs, ABs, and GDXE*

We have determined the mean EW$_{6.40}$, EW$_{6.68}$, and EW$_{6.97}$, with respective values of 169 ± 5 eV, 118 ± 5 eV, and 60 ± 4 eV for mCVs, 82 ± 7 eV, 451 ± 10 eV, and 167 ± 9 eV for non-mCVs, and 28 ± 5 eV, 327 ± 8 eV, and 45 ± 6 eV for ABs, respectively (Model A, table 3). These EWs are consistent with, but are more accurate with smaller errors than the previous reports. We further detected the Ni XXVII-Heα, Fe XXV-Heβ, and Fe XXVI-Lyβ lines in the mCVs spectrum, and Ni XXVII-Heα and Fe XXV-Heβ lines in the non-mCVs and ABs spectra for the first time.

We have also obtained high-quality spectra of the GDXE, and accurately determined EW$_{6.40}$, EW$_{6.68}$, and EW$_{6.97}$. In addition, we detect many K-shell lines of iron and nickel such as Ni I-Kα, Ni XXVII-Heα, Fe XXV-Heβ, Fe XXVI-Lyβ, Fe XXV-Heγ and Fe XXVI-Lyγ lines from the GCXE spectra. From the GBXE and GRXE spectra, newly detected lines are Ni XXVII-Heα, Fe XXV-Heγ, and Fe XXVI-Lyγ.

The EW$_{6.40}$, EW$_{6.68}$, and EW$_{6.97}$ of mCVs, non-

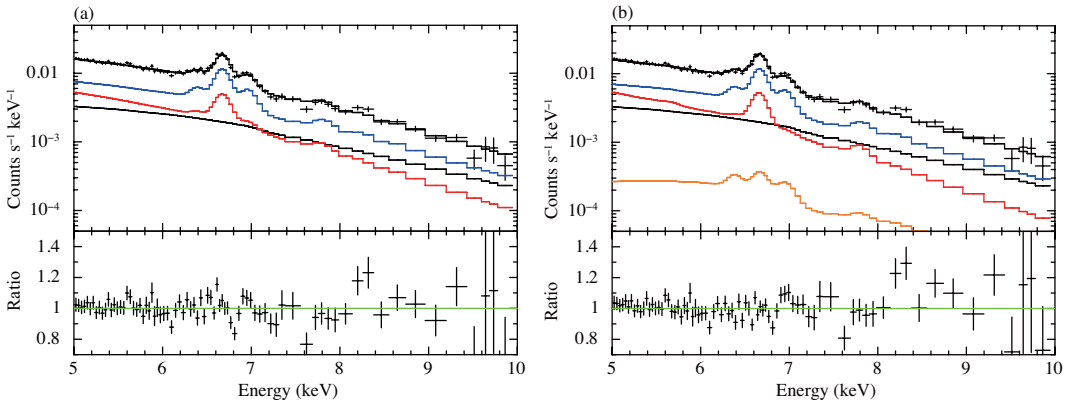

Figure 9. (a) GBXE spectrum fitted with the combination of the mCVs (orange), non-mCVs (blue), and ABs (red) of the Model A. In this case, mCVs rarely contributes the 5–10 keV spectrum. The black solid curve shows the CXB model. (b) Same as the left panel, but fitted with the Model B.

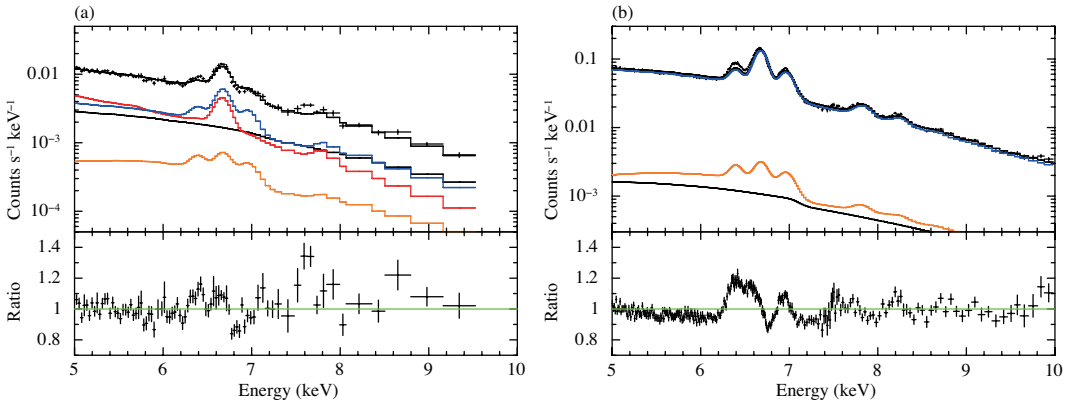

Figure 10. (a) GRXE spectrum fitted with the combination of the mCVs (orange), non-mCVs (blue), and ABs (red) of the Model B. The black solid curve shows the CXB model. (b) Same as (a), but for the GCXE.

mCVs, and ABs have been reported by several authors, mainly with *ASCA*, *Chandra*, *XMM-Newton* and *Suzaku* (Yamauchi et al. 2016 and references therein). However, the mean values of the EWs have large errors, except for Xu et al. (2016), and have large variations from author to author and/or from instrument to instrument. These large systematic errors would be due to different analysis processes from author to author for the rather faint iron K-shell structures: different instrument, different criteria of the data selections, reductions, the NXB estimations, different analysis tools, and the various other conditions.

We have estimated the EWs using the same instrument (XIS) with unified data reduction and analysis for all the GDXE, mCVs, non-mCVs, and ABs spectra. Therefore, the systematic errors of EWs, in particular relative systematic errors of EWs among the GCXE, GRXE, GBXE, mCVs, non-mCVs, and ABs would be far smaller than those of the previous reports. This is essential for the reliable reconstruction of the GCXE, GRXE, and GBXE spectra by the combination of the mean spectra of mCVs, non-mCVs, and ABs.

4.2. *Galactic Bulge X-ray Emission (GBXE)*

Using the deep *Chandra* observations (∼1 Ms) at $(l_*, b_*) = (0°.1, -1°.4)$, Revnivtsev et al. (2009); Hong (2012) made the plot of the integrated point source flux (6.5–7.1 keV) as a function of the threshold luminosity (2–10 keV). They concluded that more than ∼80% flux of the central region is resolved into point sources (figure 3b of Hong 2012). However, a problem is that number fractions (observed XLF) of CVs and ABs are significantly different between these two authors.

The high-quality GBXE and point source (mCVs, non-mCVs, and ABs) spectra with accurate $EW_{6.40}$, $EW_{6.68}$, and $EW_{6.97}$ obtained in this paper enable us to adopt a different approach to the point source origin for the GBXE. The GBXE spectrum, particularly the $EW_{6.40}$, $EW_{6.68}$, and $EW_{6.97}$and relative ratio, are well reproduced by the combined model of mCVs, non-mCVs, and ABs (figure 9). This is consistent with the point source origin proposed by Revnivtsev et al. (2009); Hong (2012). The major fraction is occupied by non-mCVs, in contrast to Revnivtsev et al. (2009); Hong (2012).

The scale heights (SHs) of the Fe I-Kα ($SH_{6.40}$), Fe XXV-Heα ($SH_{6.68}$) and the Fe XXVI-Lyα ($SH_{6.97}$) are $\sim$ 150 pc, $\sim$300 pc, and $\sim$300 pc, respectively (Yamauchi et al. 2016). These SHs are consistent with those of the mCVs, non-mCVs, and ABs, which also supports that the origin of GBXE is assembly of point sources, mainly non-mCVs (for Fe XXV-Heα, Fe XXVI-Lyα, and the 5-10 keV band flux), partly mCVs (for Fe I-Kα) and ABs (for Fe XXV-Heα). The residual at $\sim$ 8.3 keV corresponds to Fe XXV-Heγ and/or Fe XXVI-Lyβ, which will be discussed in section 4.4.

4.3. *Galactic Ridge X-ray Emission (GRXE)*

Ebisawa et al. (2005) resolved $\sim$10% of the GRXE flux into point sources above the detection threshold of $\sim 2 \times 10^{31}$ erg s^{-1} (2–10 keV) in the deepest observation of the GRXE field at $(l_*, b_*) \sim (28^\circ.5, -0^\circ.0)$. The resolved fraction of the same region by Revnivtsev & Sazonov (2007) is about 20% above the detection threshold of $\sim 10^{31}$ erg s^{-1} (1–7 keV). These differences are hard to be absorbed by the difference of the detection threshold, and hence may be regarded as a systematic error in the estimation of point source fraction.

We have obtained the high-quality GRXE spectrum, which includes the Fe I-Kα, Fe XXV-Heα, Fe XXVI-Lyα, Fe I-Kβ, Ni XXVII-Heα, Fe XXV-Heγ, and Fe XXVI-Lyγ lines. Unlike the GBXE, the GRXE spectrum cannot be well fitted with any combination of mCVs, non-mCVs and ABs (χ^2/d.o.f.= 282/91). Large excesses are found at the Fe I-Kα and Fe XXV-Heα lines (figure 10a). Taking the continuum flux into account, we estimated that the Fe I-Kα and Fe XXV-Heα fluxes of the GRXE are $\sim$ 2 and 1.2 times larger than that estimated from the best-fit combined model of mCVs, non-mCVs, and ABs.

The scale height of $SH_{6.40}$, $SH_{6.68}$, $SH_{6.97}$, and that of the 5–10 keV band flux of the GRXE are significantly smaller than those of the GBXE, and are inconsistent or marginal to those of mCVs, non-mCVs, and ABs (Yamauchi et al. 2016). These are consistent with that the GRXE cannot be reproduced by any combination of mCVs, non-mCVs nor ABs. The largest residual is found at Fe I-Kα line. The $SH_{6.40}$ of the GRXE of $\sim$70 pc is similar to molecular clouds (Yamauchi et al. 2016). Since the Fe I-Kα line shows local enhancements on the Galactic ridge, they argued that a significant fraction of Fe I-Kα is due to local bombardment of the low-energy cosmic rays (LECRs) to the molecular clouds. As for the origin of LECRs, Tanuma et al. (1999) proposed reconnections of the magnetic field which is magnified by the possible turbulent motion of gas in the Galactic ridge. This process may also produce a high-temperature plasma, and hence would compensate the deficiency of the Fe I-Kα and Fe XXV-Heα lines in the combined model (figure 10a). The origin of the residual at $\sim$ 7.6 keV is discussed in section 4.4.

4.4. *Galactic Center X-ray Emission (GCXE)*

In the deepest observation ($\sim$600 ksec exposure) near the Galactic center of the $17' \times 17'$ field around Sgr A* (40×40 pc), Muno et al. (2003) resolved $\sim$10% of the total flux (2–8 keV band) into point sources above the threshold luminosity of $\sim 10^{31}$ erg s^{-1}. In the region 2′–4′ west from Sgr A* ($\sim$900 ksec), Revnivtsev et al. (2007) resolved $\sim$40% of the flux (4–8 keV band) into point sources above the same threshold luminosity ($\sim 10^{31}$ erg s^{-1}). This fraction corresponds to $\sim$25–30% in the 2–8 keV band in the XLF of Revnivtsev et al. (2009). Thus, these two results are inconsistent with each other, which may be either due to spatial fluctuations or more likely due to large systematic errors in deriving the flux of very faint point sources, as are discussed in the previous sections.

Uchiyama et al. (2011) reported that the longitude profile of the Fe XXV-Heα line flux is at least two times larger than that of the SMD with the assumption that all the GRXE and GBXE are due to point sources (stars). The SMD is determined by the infrared observations made from the COBE/DIRBE data in the LAMBDA archive[2], IRAS and IRT (Launhardt et al. 2002; Muno et al. 2006). The similar Fe XXV-Heα excess in the GCXE region is confirmed by the direct infrared star-counting observation of the SIRIUS by Yasui et al. (2015).

The $EW_{6.40}$, $EW_{6.68}$ and $EW_{6.97}$ of the GCXE are all larger than those of mCVs, non-mCVs, and ABs (tables 3 and 1). In fact, the fit of the GCXE spectrum by a combination of the mCV, non-mCV and AB spectra is completely rejected with the large excesses in the Fe I-Kα, Fe XXV-Heα, and Fe XXVI-Lyα lines (figure 10b). The Fe I-Kα, Fe XXV-Heα, and Fe XXVI-Lyα fluxes of the GCXE (table 1) are, respectively, $\sim$2.0, 1.2, and 1.3 times larger than those estimated from the best-fit combined model (Model B). These excess ratios (relative flux) are larger than possible systematic relative errors, and hence the excesses of iron lines are robust results.

The Fe I-Kα line is due to cold gas, while the Fe XXV-Heα and Fe XXVI-Lyα lines are attributable to hot plasma. Thus, a significant contribution of additional components is required regardless of whether diffuse or other point sources. This component should emit stronger K-shell lines of iron than any other known categories, and simultaneously satisfy apparently opposite characteristics: excess of cold gas (Fe I-Kα) and that of hot plasma (Fe XXV-Heα and Fe XXVI-Lyα).

[2] http://lambda.gsfc.nasa.gov

The scale height of $SH_{6.40}$, $SH_{6.68}$, $SH_{6.97}$, and that of the 5–10 keV band flux of the GCXE are all similar to $\sim$ 30–35 pc (Yamauchi et al. 2016). These are far smaller than those of mCVs, non-mCVs and ABs, and are more like that of the central molecular zone (CMZ) (Tsuboi et al. 1999; Wienen et al. 2015). Therefore, the origin of the GCXE may be closely related to the CMZ. Near Sgr A* ($|l_*| \lesssim 0^\circ.3$), the longitude profile of Fe XXV-Heα in the east (positive l_*) shows a significant excess over the west, even if we exclude the bright supernova remnant Sgr A East. This excess would be due to larger populations of high-mass stars in the east than the west (Park et al. 2004; Muno et al. 2004; Koyama et al. 2007d). These high-mass stars may contribute to the GCXE by possible starburst activity and frequent supernova in the CMZ. Another possibility would be magnetic reconnection in the CMZ with strong magnetic field, similar to the GRXE (Tanuma et al. 1999).

Big out-bursts of Sgr A* in the past (Inui et al. 2009; Terrier et al. 2010; Ponti et al. 2010; Capelli et al. 2012) would make a very hot plasma and LECRs, which may make ionized irons higher than that in normal plasmas near the GC. Then the transitions of highly excited level (n >2) to the ground state (n = 1) are more enhanced compared to the CIE plasma. Line-like residuals at $\sim$7.8–7.9 keV and $\sim$8.2–8.3 keV, would be such enhanced iron lines. Nakashima et al. (2013) discussed a possible effect of past big flares of Sgr A* on a plasma spectrum at the south of the GC. The residual at $\sim$ 7.6 keV found in the GCXE and GRXE corresponds to Ni I-Kα, because unlike Fe I-Kα and Fe I-Kβ, Ni I-Kα is not included in the Model B spectra.

5. SUMMARY

The summary for the origin of the GDXE based on the equivalent widths and scale heights of iron K-shell lines of the GCXE, GRXE, GBXE, mCVs, non-mCVs, and ABs are as follows;

- Equivalent width of the iron K-shell lines ($EW_{6.40}$, $EW_{6.68}$, and $EW_{6.97}$) and their intensity patterns are different between the GCXE, GRXE and GBXE.

- The X-ray spectrum near the iron K-shell lines of the GBXE is well explained by the non-mCVs dominant plasmas with small contribution of mCVs and ABs.

- The X-ray spectrum near the iron K-shell lines of the GRXE shows significant excess at 6.4 keV line ($EW_{6.40}$) from any combination of mCVs, non-mCVs, and ABs. The excess of $EW_{6.40}$ is likely due to low energy cosmic protons.
- The X-ray spectrum of the GCXE shows significant excesses of Fe I-Kα, Fe XXV-Heα, and Fe XXVI-Lyα from any combination of mCVs, non-mCVs, and ABs. Therefore, significant fraction of GCXE is not due to mCVs, non-mCVs, and ABs. A possible origin would be diffuse emission produced by high activity near the GC, such as the past big flares of Sgr A*.

The authors are grateful to all members of the *Suzaku* team who provide us with the excellent spectral data. This work is supported in part by the Grant-in-Aid for Scientific Research of the Ministry of Education, Science, Sports, and Culture (No. 15H02090, MN; No. 24540232, SY; No. 24540229, KK). KKN is supported by Research Fellow of Japan Society for the Promotion of Science for Young Scientists.

REFERENCES

Byckling, K., Mukai, K., Thorstensen, J. R., & Osborne, J. P. 2010, MNRAS, 408, 2298
Capelli, R., Warwick, R. S., Porquet, D., Gillessen, S., & Predehl, P. 2012, A&A, 545, A35
Cunha, K., Sellgren, K., Smith, V. V., et al. 2007, ApJ, 669, 1011
Ebisawa, K., Tsujimoto, M., Paizis, A., et al. 2005, ApJ, 635, 214
Hong, J. 2012, MNRAS, 427, 1633
Inui, T., Koyama, K., Matsumoto, H., & Tsuru, T. G. 2009, PASJ, 61, S241
Koyama, K., Awaki, H., Kunieda, H., et al. 1989, Nature, 339, 603
Koyama, K., Maeda, Y., Sonobe, T., et al. 1996, PASJ, 48, 249
Koyama, K., Tsunemi, H., Dotani, T., et al. 2007a, PASJ, 59, S23
Koyama, K., Inui, T., Hyodo, Y., et al. 2007b, PASJ, 59, S221
Koyama, K., Uchiyama, H., Hyodo, Y., et al. 2007c, PASJ, 59, S237
Koyama, K., Hyodo, Y., Inui, T., et al. 2007d, PASJ, 59, S245
Kushino, A., Ishisaki, Y., Morita, U., et al. 2002, PASJ, 54, 327
Launhardt, R., Zylka, R. & Mezger, P. G. 2002, A&A, 384, 112
Muno, M. P., Baganoff, F. K., Bautz, M. W., et al. 2003, ApJ, 589, 225
Muno, M. P., Baganoff, F. K., Bautz, M. W., et al. 2004, ApJ, 613, 326
Muno, M. P., Bauer, F. E., Bandyopadhyay, R. M., & Wang, Q. D. 2006, ApJS, 165, 173
Nakajima, H., Tsuru, T. G., Nobukawa, M., et al. 2009, PASJ, 61, S233
Nakashima, S., Nobukawa, M., Uchida, H., et al. 2013, ApJ, 773, 20
Neustroev, V. V. & Zharikov, S. 2008, MNRAS, 386, 1366

Nobukawa, M., Koyama, K., Tsuru, T. G., Ryu, S. G., & Tatischeff, V. 2010, PASJ, 62, 423
Park, S., Muno, M. P., Baganoff, F. K., et al. 2004, ApJ, 603, 548
Pandey, J. C. & Singh, K. P. 2012 MNRAS, 419, 1219
Patterson, J. 1984, ApJS, 54, 443
Ponti, G., Terrier, R., Goldwurm, A., Belanger, G., & Trap, G. 2010, ApJ, 714, 732
Reid, M. J. & Brunthaler, A. 2004, ApJ, 616, 872
Revnivtsev, M. G., Sazonov, S., Gilfanov, M., Churazov, E., & Sunyaev, R. 2006a, A&A, 452, 169
Revnivtsev, M. G., Molkov, S., & Sazonov, S. 2006b, MNRAS, 373, L11
Revnivtsev, M. & Sazonov, S. 2007, A&A, 471, 159
Revnivtsev, M., Vikhlinin, A., & Sazonov, S. 2007, A&A, 473, 857
Revnivtsev, M., Sazonov, S., Churazov, E., et al. 2009, Nature, 458, 1142
Sakano, M., Koyama, K., Murakami, H., Maeda, Y., & Yamauchi, S. 2002, ApJS, 138, 19
Sazonov, S., Revnivtsev, M., Gilfanov, M., Churazov, E. & Sunyaev, R. 2006, A&A, 450, 117
Serlemitsos, P. J., Soong, Y., Chan, K., et al. 2007, PASJ, 59, S9
Sheets, H. A., Thorstenaen, J. R., Peters, C. J., Kapusta, A. B. & Taylor, C. J. 2007, PASP, 119, 494
Tanuma, S., Yokoyama, T., Kudoh, T., et al. 1999, PASJ, 51, 161
Tawa, N., Hayashida, K., Nagai, M., et al. 2008, PASJ, 60, S11
Terrier, R., Ponti, G., Bélanger, G., et al. 2010, ApJ, 719, 143
Tsujimoto, M., Hyodo, Y. & Koyama, K. 2007, PASJ, 59, S229
Tsuboi, M., Handa, T. & Ukita, N. 1999, ApJS, 120, 1
Uchiyama, H., Nobukawa, M., Tsuru, T. G., Koyama, K., & Matsumoto, H. 2011, PASJ, 63, S903
Uchiyama, H., Nobukawa, M., Tsuru, T. G., & Koyama, K. 2013, PASJ, 65, 19
Vaiana, G. S., Cassinelli, J. P., Fabbiano, G., et al. 1981, ApJ, 245, 163
Wargelin, B. J., Beiersdorfer, P., Neill, P. A., Olson, R. E., & Scofield, J. H. 2005, ApJ, 634, 687
Warwick, R. S. 2014, MNRAS, 445, 66
Wienen, M., Wyrowski, F., Menten, K. M., et al. 2015, A&A, 579, 91
Worrall, D. M., Marshall, F. E., Boldt, E. A., & Swank, J. H. 1982, ApJ, 255, 111
Xu, X., Wang, Q. D., & Li, X. 2016, ApJ, 818, 136
Yamauchi, S. & Koyama, K. 1993, ApJ, 404, 620
Yamauchi, S., Ebisawa, K., Tanaka, Y., et al. 2009, PASJ, 61, S225
Yamauchi, S., Nobukawa, K. K., Nobukawa, M., Uchiyama, H., & Koyama, K. 2016, PASJ, 68, 59
Yasui, K., Nishiyama, S., Yoshikawa, T., et al. 2015, PASJ, 67, 123
Yuasa, T., Makishima, K., & Nakazawa, K. 2012, ApJ, 753, 129